Title

Computational analysis of six optical coherence tomography systems for vocal fold imaging: A comparison study

Journal

Lasers in Surgery and Medicine, 51(5)

ISSN

1050-9267

Authors

Pham, Tiffany T

Chen, Lily

Heidari, Andrew E

et al.

Publication Date

2019-07-01

DOI

10.1002/lsm.23060

Peer reviewed

HHS Public Access

Author manuscript

Lasers Surg Med. Author manuscript; available in PMC 2020 July 25.

Computational Analysis of Six Optical Coherence Tomography Systems for Vocal Fold Imaging: A Comparison Study

Tiffany T. Pham, MS[1,2], **Lily Chen, BS**[1], **Andrew E. Heidari, PhD**[1,3], **Jason J. Chen, BS**[1,3], **Alisa Zhukhovitskaya, MD**[1,4], **Yan Li, MS**[1,3], **Urja Patel**[1], **Zhongping Chen, PhD**[1,3], **Brian J.F. Wong, MD, PhD**[1,2,3,4,*]

[1]Beckman Laser Institute & Medical Clinic, University of California—Irvine, Irvine, California 92612

[2]School of Medicine, University of California—Irvine, Irvine, California 92617

[3]Department of Biomedical Engineering, University of California—Irvine, Irvine, California 92697

[4]Department of Otolaryngology—Head and Neck Surgery, University of California—Irvine, Orange, California 92868

Abstract

Objectives: There have been many advancements in laryngeal imaging using optical coherence tomography (OCT), with varying system design and probes for use in research, office, and operating room settings. We evaluated the performance of six distinct OCT systems in imaging porcine vocal folds (cords) using computational image processing and segmentation.

Methods: Porcine vocal folds were scanned using six OCT systems. Imaging system and probe performance were quantitatively assessed for signal penetration, layer differentiation, and epithelium (EP) measurement. Fitted exponential decay curves with corresponding α constant and intensity thresholding segmentation were utilized to quantify the aforementioned parameters.

Results: The smallest average α constant and deepest signal penetration was of the SS-OCT 1700 nm 90 kHz microscope system (α= −1.74), followed by the SS-OCT 1310 nm 200 kHz VCSEL microscope system (α= −1.99), and SS-OCT 1310 nm 50 kHz rigid forward viewing endoscope system (α= −2.23). The EP was not readily visualized for three out of six systems, but was detected using automated segmentation. Average EP thickness (mean ± SD) was calculated as 55.79 ± 31.86 mm which agrees favorably with previous literature.

Conclusion: Comparisons of OCT systems are challenging, as they encompass different probe design, optical path, and lasers, depending on application. Practical evaluation of different systems using computer based quantitative image processing and segmentation revealed basic, constructive information, such as EP measurements. To further validate the comparisons of system performance with clinical usability, *in vivo* human laryngeal imaging will be conducted. Further

*Correspondence to: Brian J.F. Wong MD, PhD, Beckman Laser Institute & Medical Clinic, University of California—Irvine, Irvine, CA 92612. bjwong@uci.edu.

Conflict of Interest Disclosures: All authors have completed and submitted the ICMJE Form for Disclosure of Potential Conflicts of Interest and have disclosed the following: Dr. Zhongping Chen has financial interests with OCT Medical Inc., which however does not support this work.

development of automated image processing and segmentation can be useful in rapid analysis of information. Lasers Surg. Med.

Keywords

larynx; vocal folds; true vocal folds; vocal cords; porcine vocal folds; optical coherence tomography; laryngeal imaging; system comparisons; segmentation

INTRODUCTION

Evaluation of the larynx and vocal folds (i.e., vocal cords, true vocal folds [TVFs]) requires specialized hardware, as they cannot be visualized directly during standard physical examination. The development of laryngeal visualization and imaging has incrementally advanced over three centuries. Otolaryngologists currently evaluate the larynx using a dental mirror and headlamp, flexible fiber-optic, or rigid endoscope. However, these conventional methods cannot capture subsurface composition of the TVFs and associated pathologies. State-of-the-art clinical imaging includes videostroboscopy supplemented by videokymography, high-speed videolaryngoscopy with or without narrow band imaging, or depth-kymography, but their uses are uncommon in general practice [1–5]. Although these technologies functionally analyze the laryngeal mucosal wave during phonation, they still only assess the surface. Dynamic magnetic resonance imaging has recently been introduced to measure laryngeal structures and glottal parameters with multiplanar high-resolution imaging. However, it still has insufficient resolution to classify TVF lesions. Thus, the challenge remains to study cross-sectional TVF structure and pathology without invasive biopsy and histological analysis [6].

Optical Coherence Tomography (OCT), a minimally invasive imaging technology, is capable of producing near histopathological images of biological tissues [7]. There are several OCT system configurations: time domain (TD), and Fourier domain techniques including swept source (SS) and spectral domain (SD) [8–10]. Based upon system configuration, various low coherent near-infrared light sources are used, including super luminescent diodes (SLD) [8] and swept vertical cavity surface emitting lasers (VCSELs) [11]. Various OCT probes and hand piece designs—including microscopes, rigid endoscopes, and flexible endoscopes—allow for forward viewing [8,12–25], side viewing [11,26–32], or rotary viewing [33,34]. Using a TD system with a forward facing probe, Sergeev et al. first demonstrated the feasibility of using endoscopic OCT to image the mucosa of various organs, including the larynx [17]. Since then, many OCT systems have been developed for intraoperative and in-office use. Small dual channel nasolaryngeal endoscopic OCT has been developed to image normal and suspicious lesions in awake patients [16,26]. Advancements in image acquisition speed and phase stability of laryngeal endoscopic OCT has allowed for acquisition of functional information during phonation and vocal fold vibration [11,27]. Furthermore, OCT imaging systems have been integrated into surgical microscopes for hands-free image acquisition during direct laryngoscopy [14,15,20,24].

Although varied quality of images produced have been documented, objective comparisons of multiple OCT imaging systems for laryngeal imaging have not been performed.

Comparisons in literature predominantly evaluate two systems. Variable light sources, optical probe design, and interferometry components complicate system comparisons. Imaging performance theoretically should depend upon laser center wavelength and individual system components. However, in practice, there are additional factors to consider. The variability in the manufacture's specifications of optical components and their arrangement could affect the overall performance, creating difficulties in comparisons.

Furthermore, objective assessment presents a challenging task given the variable subjective human interpretation of OCT images and their relative quality. The human eye is not well-suited to observe subtle differences in pixel intensity variations that mark the edges between layers. OCT image interpretation often is subjective based upon what the observer expects to see rather than what is truly represented in the image data. The use of segmentation algorithms for OCT imaging has been established and has the potential to aid in rapid and objective data analysis that may not be attained by visual interpretation [19,35].

Thus, we aim to compare six OCT systems in imaging *ex vivo* porcine TVFs, using quantitative image processing and segmentation algorithms.

MATERIALS AND METHODS

Tissue Specimens

Freshly excised porcine larynx (Fig. 1) (obtained from a local abattoir) was fixed in formalin (formalin refractive index, $n = 1.37$) to maintain structural integrity of the tissue, and subsequently imaged using the six OCT systems consecutively. As device setup can be time consuming and fresh tissue undergoes autolysis, fixed tissue was utilized [21,29]. The sample was bisected between the two TVFs to allow access to the structures.

Image Acquisition

Imaging systems with various scanning probe embodiments were compared (Fig. 2). Two flexible probe systems, two gradient-index (GRIN) lens rigid endoscopes, and two microscope systems were evaluated. The specifications of each system and probe are displayed in Table 1. Two-dimensional OCT images of the central area of TVFs were acquired and adapted to accommodate the field of view (FOV) and capabilities of each system. All systems and probes imaged the superior surface of the TVFs, apart from the SS-OCT 1310 nm 50 kHz flexible side viewing rotational endoscope system. Due to its scanning geometry, this system was only reliable to image the medial surfaces of the TVF.

Visual Assessment

OCT images were visually assessed for overall TVF morphology as attained by each system. Clarity of layered structure was based on a scale of "visible," "moderately visible," and "not visible."

Image Processing

OCT B-scans acquired with each system were analyzed by image processing algorithms to assess penetration depth, and contrast of tissue microstructures (epithelium [EP], lamina

propria [LP], and basement membrane [BM]), and EP thickness. The EP is the most superficial layer. The superficial lamina propria (SLP) is denoted by an increase in pixel intensity, specifying a second layer and the deep lamina propria (DLP) is the third layer. The BM is the interface between the EP and SLP.

Intensity Threshold Segmentation

To obtain EP thickness, a semi-automated Python (Python Software Foundation, Wilmington, DE) image processing program denoised, segmented, and calculated the average EP thickness (schematic, Fig. 3). First, data was converted to grayscale images in ImageJ (LOCI, Madison, WI) [36]. Using 8–85 representative B-scans—system dependent—a user defined region of interest (ROI) of the TVF was selected. Briefly, ROIs were denoised by the scikit-image implementation [37] of the total variation denoising Split-Bregman method [38]. By sampling pixel luminance, a pixel intensity histogram was produced. Splines smoothed the histogram to identify threshold intensity values by which EP, SLP, and noise could be separated. For each respective layer, threshold values were deduced from the observation that noise generally exhibited the lowest centered distribution of intensities, SLP with the highest centered intensity distribution, and EP centered in between the former two. Two intensity values were identified to separate the intensity histogram of the B-scan into three intensity value ranges. Using these two values, the EP contour was obtained using the marching squares algorithm implemented in scikit-image [39]. The vertical height of the segmented epithelial boundaries was calculated for all A-lines within each contour, and mean thickness was subsequently determined.

Alpha Constant (α)

Average intensity based exponential decay curves and respective α constants (α) were calculated to compare OCT signal depth penetration and contrast of signal intensity into the LP [40,41]. The α constant is defined as the decay constant of the fitted first order exponential decay to the OCT intensity data. A MATLAB (MathWorks, Natick, MA) image processing script was created to calculate the average α constants in all given A-lines in the ROI. The algorithm (schematic, Fig. 4) is a modified form of decay fitting of intensity signals [41]. Briefly, a user-defined ROI in a representative OCT B-scan was selected to assess the same area of the TVFs. Next, tissue layers were contoured using the previously described intensity threshold segmentation approach [35]. Data from the EP was removed, and the LP surface was then shifted to a line to simplify further processing. All A-lines captured within the ROI were then laterally averaged to reduce speckle artifact. Lastly, a first order exponential decay was fitted to the depth resolved intensity OCT data and an average α constant was determined.

RESULTS

ROIs of OCT images acquired from each system are represented in Figure 5. The yellow arrow denotes the EP, the purple asterisk denotes the BM, the blue arrow denotes the SLP, and the orange arrow denotes the DLP. As seen in Figure 5a, the image produced by the SS-OCT 1310 nm 200 kHz VCSEL microscope system shows clear visibility of the BM and boundary between the SLP and DLP, but poor visibility of the EP. The high intensity SLP

layer is clearly separable from the LP layer. The ROI surrounding the TVF was obtained from a B-scan depicting a large FOV, best observed by the varying heights of the tissue surface morphologically. The SS-OCT 1700 nm 90 kHz microscope system shown in Figure 5c has a similar FOV and is able to clearly differentiate the BM, SLP, and DLP. Once again it is very challenging to visualize the thin EP above the BM. The SLP is of lower intensity compared to the DLP with good layer differentiation. The SS-OCT 1310 nm 50 kHz side viewing rotational endoscope system seen in Figure 5e can resolve the structure between the EP, BM, SLP, and DLP, with the SLP having the highest intensity. Adequate contrast for differentiation of the LP is noted, however the EP, although visible, is difficult to appreciate. It should be noted that the tissue is curved due to the side viewing rotational scanning geometry. The image produced by the TD-OCT 1310 nm 254 Hz flexible forward viewing endoscope system is seen in Figure 5g. The EP, BM, SLP, and DLP are clearly distinguishable. The contrast for layer differentiation is moderate. The SLP shows the highest intensity. The tissue appears to be flat due to the short scanning FOV provided by the probe (2 mm). The imaged acquired by the SS-OCT 1310 nm 50 kHz rigid forward viewing endoscopy system (Fig. 5i) cannot resolve the EP or BM visually. However, the SLP and DLP layers are visible with moderate differentiation. Tissue structure is flat and angled due to the limited FOV (3 mm). Lastly, the SS-OCT 1310 nm 200 kHz VCSEL rigid side viewing endoscope system has the largest FOV, as reflected by the capability of imaging the curvature of TVFs as can be seen in Figure 5k. The EP, BM, SLP, and DLP are visible with moderate layer differentiation. These visual assessments are summarized in Table 2.

Segmentation performed using image intensity thresholding is also presented in Figure 5. The yellow contour delineates the epithelial layer detectable by the Python algorithm. Average EP thickness and standard deviation (SD) for each of the six OCT imaging systems are summarized in Table 3 and Figure 6. Values for average EP thickness ranged from 45.73 μm for the SS-OCT 1310 nm 50 kHz flexible size viewing endoscope system to 76.27 μm for the SS-OCT 1310 nm 200 kHz VCSEL rigid side viewing system. Average EP thickness (±SD) across all systems was calculated to be 55.79 ± 31.86 mm. The EP was not readily identified by visual inspection of each image for all OCT systems, but was measured *via* this segmentation algorithm.

Average intensity based exponential decay curves and the corresponding α constants for images acquired by each OCT imaging system are shown in Figure 7 and listed in Table 2. The alpha decay curves provided a quantitative measure of depth penetration. The smallest average α constant was of the SS-OCT 1700 nm 90 kHz microscope system ($\alpha = -1.74$), followed by the SS-OCT 1310 nm 200 kHz VCSEL microscope system ($\alpha = -1.99$), and SS-OCT 1310 nm 50 kHz rigid forward viewing endoscope system ($\alpha = -2.23$).

DISCUSSION

As the anatomy and dynamic nature of the upper airway make imaging the vocal folds a challenge, many different approaches to OCT laryngeal imaging have been developed. However, there have been no comparisons of systems concurrently, which was the motivation for this study.

While in theory, source specifications and tissue optical properties should predict to a degree the α constant and image quality, image acquisition results vary depending on many factors related to device design. This includes the collection efficiency of the probe's optics, probe depth of focus, the *quantum* efficiency and frequency response of the photodetector, and the position of the sample with respect to the focus. Most OCT systems are bespoke and application specific, where the clinical needs dictate the wavelength and type of probe utilized. For instance, a side viewing rotational endoscope is well utilized for a luminal organ, while a forward viewing endoscope is better employed for biopsy guidance, device placement, or uses in which a large distance between the OCT probe and tissue surface is needed [42]. Due to this variability, side-by-side comparisons of these systems are challenging. For instance, imaging the exact location of the TVFs at micron level precision is challenging, as each probe design and FOV is slightly different. Difficulties in focus spot consistency amongst systems made comparisons challenging as different wavelengths and probes each have unique depth-of-focus. Despite the aforementioned practical limitations, it is important to provide a functional evaluation of these different OCT systems. This study's strengths are in the diversity of the six different system designs compared and the constructive information produced, which provides insight towards what an ideal system may be for laryngeal imaging.

With system differences in mind, objective comparisons were carried out to garner information from these OCT images. Due to the thin porcine EP in the TVF and the given axial resolution of the OCT systems, it is challenging to observe the EP layer in most images with the naked eye, without sufficient contrast. This can be explained by the subjective visual misinterpretations of where the EP and LP boundaries reside. The EP is a thin, homogenous, low intensity layer above the thicker, heterogenous, higher intensity SLP layer filled with loose connective tissue and glandular structures [29]. The EP was not readily visible in three out of six systems (Table 2), but was quantitatively analyzed and detected using the computational methods. Using a standardized image segmentation method, the variability of subjective interpretation between imaging systems can be mitigated and useful information on layer thickness and geometry is obtained from these images. Our segmentation algorithm provided a reliable and consistent estimate of EP thickness for most systems (range 45.73–76.27 μm) with the overall average (±SD) of six systems as 55.79 ± 31.86 mm, which agrees well with values from literature. The porcine TVFs have documented EP thicknesses of 30–190 μm [21,22,29,43]. Given the homogeneity of the TVF, the SD for each system can also be a useful indicator for system performance. The SS-OCT 1310 nm 200 kHz microscope system and SS-OCT 1700 nm 90 kHz microscope system have the smallest SD values indicating a reproducible imaging plane. The small SD values can be attributed to the stationary aspect of the microscope platform, as compared to the bulk motion artifact from hand held endoscopes. Future studies in live subjects should consider motion artifacts: involuntary motion of the TVFs, motion of the subject's body, and motion of the user and the probe, which may all limit OCT image quality. With the addition of adaptive optics and real time surface tracking for dynamic focusing, future improvements can be made to accurately measure the stratified structure.

Exponential decay curves also provide some insight on depth penetration between the systems. The α constant of the SS-OCT 1700 nm 90 kHz microscope system (−1.74) was

found to be smaller than the SS-OCT 1300 nm 200 kHz VCSEL microscope system (−1.99), which by value indicates a slower signal roll off and deeper penetration for the 1700 nm system. It is well understood that light diffusion into a turbid medium such as biological tissue, is governed by light scattering and absorption. The literature has documented the advantages of a 1700 nm center wavelength SS laser which preferentially produces a larger degree of forward scattering photons rather than side or back scattering photons in turbid tissue [40,44–47]. However, high bandwidth detectors capable of efficiently detecting 1700 nm photons are in their infancy, and at present have relatively low *quantum* efficiency. Due to limited availability of optically efficient wide band frequency response balanced detectors for the 1700 nm OCT system, interferometer components were not optimized for use by this system, which could have limited some penetration depth or signal bandwidth detection. To achieve better imaging results, the laser, analog to digital data acquisition card, and detector should all be paired together to optimize the digital signal processing pathway of the OCT interferogram.

The SS-OCT 1310 nm 50 kHz side viewing flexible rotational endoscope system provides adequate tissue layer differentiation and depth penetration with a small α constant. However, it should be noted that the α constant for a side-viewing helical scanning probe could be affected by position of the probe to the tissue. The α constant may vary laterally, depending on the trajectory of the output beam with respect to the surface normal. Although microscope systems have superior lateral resolution due to the larger numerical aperture, flat planar focus field, and higher collection efficiency compared to that of endoscopic probes, they are not suitable for *in vivo* laryngeal imaging. The complicated, narrow anatomy of the upper airway does not allow for a large, forward facing lens. A slender endoscope is more useful and practical, with the tradeoff of lower axial and lateral resolution. Endoscopes typically have limited numerical aperture and only accommodate small incident beam diameters based on lens size and endoscope form factor. The lateral resolution of an endoscope is often limited compared to a microscope scanning system, which can have resolutions ranging from 1 to 30 μm [33,48,49]. In addition, endoscopes with several lenses have a large insertion loss due to the multiple reflective surfaces of the optical assembly, which affects both the axial and lateral resolutions through dispersion and chromatic aberration. Axial resolution is clinically significant to resolve BM changes in evaluating cancer. Lateral resolution can aid in the monitoring of noncancerous pathologies, or in guidance of certain types of procedures, such as steroid injections of nodules, in which differentiation of layered structure is not essential. Further optical relay optimization must be conducted to determine the most suitable lens system for the probe's form factor and performance.

Contrast between the EP and LP may be affected by the conversion and compression of the raw OCT interferogram to BMP image format. The range of values that represent the intensity distribution in the raw data may be larger than the grayscale range of values for BMP images. Although this may be a limitation, BMP files were used for practicality as the raw data was not attainable for all systems. In addition, the use of formalin fixed *ex vivo* porcine larynx can also contribute to contrast limitations. With blood and water content present in *in vivo* tissue, the absorption of the near-infrared light will be greater than that of dehydrated or fixed tissues [50,51]. Formalin increases scattering intensity from muscle

layers, as well as shrinkage of EP, muscle, and connective tissue [50]. However, according to Kimura et al., the shrinkage can be estimated: 59% in the medial-lateral direction and 40% in the inferior-superior direction [52]. Nonetheless, this study uses the same specimen with these consistent artifacts across all systems. Furthermore, although there are other animal phonation models such as the canine larynx [43], the porcine larynx is more readily available and is similar in vocal fold thickness, structure, and stiffness to the human larynx [53,54]. Previous studies have successfully used *ex vivo* or formalin fixed porcine larynx as a model for OCT laryngeal imaging and the study of vocal fold structure and function [21,22,55]. Thus, we believe imaging the *ex vivo* formalin fixed porcine larynx in this study provides useful information on system performance and the development of tools for image analysis.

This study is a practical comparison of OCT systems based on their performance in an *ex vivo* model. Apart from image quality, which depends on, but is not limited to resolution, layer differentiation, and depth penetration, other factors that are important for laryngeal imaging include the practical usability of the system and the adoption of these devices into current technologies, such as the visible light endoscope used in clinical practice. However, this study showed the ability to use image processing methods to objectively compare systems and to garner information that is not visibly acquired.

CONCLUSION

In this study, we compared six OCT imaging systems in imaging the TVFs. Analysis using segmentation algorithms garnered information that was not readily resolved by the naked eye. Although optical and tissue properties ought to predict system performance, image acquisition results vary depending on components of the system and their summation of parts. To further validate the comparisons of system performance with clinical usability, *in vivo* human laryngeal imaging will be conducted. Further development of automated image processing and segmentation can be useful in rapid analysis of information.

ACKNOWLEDGMENTS

This work was supported in part by the National Institutes of Health (R43RR026184, R01HL103764, R01HL105215, R43HD071701, R44CA177064, P41EB015890, R01HL125084, R01HL127271). The content is solely the responsibility of the authors and does not necessarily represent the official views of the National Institutes of Health.

REFERENCES

1. Maurer D, Hess M, Gross M. High-speed imaging of vocal fold vibrations and larynx movements within vocalizations of different vowels. Ann Otol Rhinol Laryngol 1996;105(12): 975–981. [PubMed: 8973285]
2. Hess MM, Gross M. High-speed, light-intensified digital imaging of vocal fold vibrations in high optical resolution via indirect microlaryngoscopy. Ann Otol Rhinol Laryngol 1993;102(7):502–507. [PubMed: 8333671]
3. Deliyski DD, Hillman RE. State of the art laryngeal imaging: Research and clinical implications. Curr Opin Otolaryngol Head Neck Surg 2010;18(3):147–152. [PubMed: 20463479]
4. Švec JG, Schutte HK. Videokymography: High-speed line scanning of vocal fold vibration. J Voice 1996;10(2):201–205. [PubMed: 8734395]

5. Volgger V, Felicio A, Lohscheller J, et al. Evaluation of the combined use of narrow band imaging and high-speed imaging to discriminate laryngeal lesions. Lasers Surg Med 2017;49(6):609–618. [PubMed: 28231400]
6. Winiarski P, Lewandowski A, Greczka G, Banaszewski J, Klimza H, Wierzbicka M. Primary and salvage laser surgery of 341 glottic cancers—Comparison of treatment outcomes between university head neck tertiary referral center and local head neck department. Lasers Surg Med 2018; 50(4): 311–318. [PubMed: 29135033]
7. Huang D, Swanson EA, Lin CP, et al. Optical coherence tomography. Science 1991;254(5035): 1178–1181. [PubMed: 1957169]
8. Rubinstein M, Fine EL, Sepehr A, et al. Optical coherence tomography of the larynx using the niris system. J Otolaryngol Head Neck Surg 2010;39(2):150–156. [PubMed: 20211101]
9. Volgger V, Sharma GK, Jing J, et al. Long-range Fourier domain optical coherence tomography of the pediatric subglottis. Int J Pediatr Otorhinolaryngol 2015;79(2): 119–126. [PubMed: 25532671]
10. Betz CS, Volgger V, Silverman SM, et al. Clinical optical coherence tomography in head & neck oncology: Overview and outlook. Head Neck Oncol 2013;5(3):35.
11. Coughlan CA, Chou LD, Jing JC, et al. In vivo cross-sectional imaging of the phonating larynx using long-range Doppler optical coherence tomography. Sci Rep 2016;6:22792. [PubMed: 26960250]
12. Luerssen K, Lubatschowski H, Ursinus K, Gasse H, Koch R, Ptok M. [Optical coherence tomography in the diagnosis of vocal folds]. HNO 2006;54(8):611–615. [PubMed: 16479385]
13. Jerjes W, Upile T, Conn B, et al. In vitro examination of suspicious oral lesions using optical coherence tomography. Br J Oral Maxillofac Surg 2010;48(1):18–25. [PubMed: 19726114]
14. Just T, Lankenau E, Prall F, Hüttmann G, Pau HW, Sommer K. Optical coherence tomography allows for the reliable identification of laryngeal epithelial dysplasia and for precise biopsy: A clinicopathological study of 61 patients undergoing microlaryngoscopy. Laryngoscope 2010;120(10): 1964–1970. [PubMed: 20824740]
15. Vokes DE, Jackson R, Guo S, et al. Optical coherence tomography-enhanced microlaryngoscopy: Preliminary report of a noncontact optical coherence tomography system integrated with a surgical microscope. Ann Otol Rhinol Laryngol 2008;117(7):538–547. [PubMed: 18700431]
16. Cernat R, Tatla TS, Pang J, et al. Dual instrument for *in vivo* and *ex vivo* OCT imaging in an ENT department. Biomed Opt Express 2012;3(12):3346. [PubMed: 23243583]
17. Sergeev A, Gelikonov V, Gelikonov G, et al. In vivo endoscopic OCT imaging of precancer and cancer states of human mucosa. Opt Express 1997;1(13):432–440. [PubMed: 19377567]
18. Kraft M, Lüerssen K, Lubatschowski H, Glanz H, Arens C. Technique of optical coherence tomography of the larynx during microlaryngoscopy. Laryngoscope 2007;117(5): 950–952. [PubMed: 17473703]
19. Wisweh H, Merkel U, Hüller A-K, Lüerβen K, Lubatschowski H. Optical coherence tomography monitoring of vocal fold femtosecond laser microsurgery. Ther Laser Appl Laser-Tissue Interact III 2007;6632_6 10.1117/12.728139.
20. Englhard AS, Betz T, Volgger V, et al. Intraoperative assessment of laryngeal pathologies with optical coherence tomography integrated into a surgical microscope. Lasers Surg Med 2017;49(5): 490–497. [PubMed: 28231390]
21. Nassif NA, Armstrong WB, De Boer JF, Wong BJF. Measurement of morphologic changes induced by trauma with the use of coherence tomography in porcine vocal cords. Otolaryngol Head Neck Surg 2005;133(6):845–850. [PubMed: 16360501]
22. Kobler JB, Chang EW, Zeitels SM, Yun SH. Dynamic imaging of vocal fold oscillation with four-dimensional optical coherence tomography. Laryngoscope 2010;120(7):1354–1362. [PubMed: 20564724]
23. Luërßen K, Lubatschowski H, Radicke N, Ptok M. Optical characterization of vocal folds using optical coherence tomography. Med Laser Appl 2006;21:185–190.
24. Just T, Lankenau E, Hüttmann G, Pau HW. Intra-operative application of optical coherence tomography with an operating microscope. J Laryngol Otol 2009;123(9):1027. [PubMed: 19243643]

25. Kraft M, Glanz H, von Gerlach S, Wisweh H, Lubatschowski H, Arens C. Clinical value of optical coherence tomography in laryngology. Head Neck 2008;30(12):1628–1635. [PubMed: 18767182]
26. Sepehr A, Armstrong WB, Guo S, et al. Optical coherence tomography of the larynx in the awake patient. Otolaryngol Head Neck Surg 2008;138(4):425–429. [PubMed: 18359348]
27. Liu G, Rubinstein M, Saidi A, et al. Imaging vibrating vocal folds with a high speed 1050nm swept source OCT and ODT. Opt Express 2011;19(12):11880–11889. [PubMed: 21716421]
28. Armstrong WB, Ridgway JM, Vokes DE, et al. Optical coherence tomography of laryngeal cancer. Laryngoscope 2006;116(7):1107–1113. [PubMed: 16826043]
29. Torkian BA, Guo S, Jahng AW, Liaw LHL, Chen Z, Wong BJF. Noninvasive measurement of ablation crater size and thermal injury after CO2laser in the vocal cord with optical coherence tomography.OtolaryngolHeadNeckSurg 2006;134(1):86–91.
30. Klein AM, Pierce MC, Zeitels SM, et al. Imaging the human vocal folds *in vivo* with optical coherence tomography: A preliminary experience. Ann Otol Rhinol Laryngol 2006;115(4):277–284. [PubMed: 16676824]
31. Burns JA, Kim KH, Johannes F, Anderson RR, Zeitels SM. Polarization-Sensitive optical coherence tomography imaging of benign and malignant laryngeal lesions: An *in vivo* study. Otolaryngol Head Neck Surg 2011;145(1):91–99. [PubMed: 21493273]
32. Kim KH, Burns JA, Bernstein JJ, Maguluri GN, Park BH, de Boer JF. In vivo 3D human vocal fold imaging with polarization sensitive optical coherence tomography and a MEMS scanning catheter. Opt Express 2010;18(14): 14644–14653. [PubMed: 20639950]
33. Zhu J,Qi L,Miao Y,et al.3Dmappingofelasticmodulususing shear wave optical micro-elastography. Sci Rep. 2016;6: 35499. [PubMed: 27762276]
34. Sharma GK, Ahuja GS, Wiedmann M, et al. Long-range optical coherence tomography of the neonatal upper airway for early diagnosis of intubation-related subglottic injury. Am J Respir Crit Care Med 2015;192(12):1504–1513. [PubMed: 26214043]
35. Qi L, Huang S, Heidari AE, et al. Automatic airway wall segmentation and thickness measurement for long-range optical coherence tomography images. Opt Express 2015;23(26):33992–34006. [PubMed: 26832057]
36. Eliceiri K, Schneider CA, Rasband WS, Eliceiri KW. NIH Image to ImageJ: 25 years of image analysis HISTORICAL commentary NIH Image to ImageJ: 25 years of image analysis. Nat Methods 2012;9(7):671–675. [PubMed: 22930834]
37. van der Walt S, Schönberger JL, Nunez-Iglesias J, et al. Scikit-image: Image processing in Python. PeerJ 2014;2: e453. [PubMed: 25024921]
38. Wang X, Yu X, Liu X, et al. A two-step iteration mechanism for speckle reduction in optical coherence tomography. Biomed Signal Process Control 2018;43:86–95.
39. Maple C. Geometric design and space planning using the marching squares and marching cube algorithms; Proceedings 2003 International Conference on Geometric Modeling and Graphics, GMAG 2003; 2003. doi:10.1109/GMAG. 2003.1219671
40. Sharma U, Chang EW, Yun SH. Long-wavelength optical coherence tomography at 1.7mm for enhanced imaging depth. Opt Express 2008;16(24):19712–19723. [PubMed: 19030057]
41. Tsai MT, Lee HC, Lee CK, et al. Effective indicators for diagnosis of oral cancer using optical coherence tomography. Opt Express 2008;16(20):15847–15862. [PubMed: 18825221]
42. Gora MJ, Suter MJ, Tearney GJ, Li X. Endoscopic optical coherence tomography: technologies and clinical applications [Invited]. Biomed Opt Express 2017;8(5):2405–2444. [PubMed: 28663882]
43. Garrett CG, Coleman JR, Reinisch L. Comparative histology and vibration of the vocal folds: implications for experimental studies in microlaryngeal surgery. Laryngoscope 2000;110(5 I):814–824. [PubMed: 10807360]
44. Li Y, Jing J, Heidari E, Zhu J, Qu Y, Chen Z. Intravascular optical coherence tomography for characterization of atherosclerosis with a 1.7 micron swept-Source laser. Sci Rep 2017;7(1):14525. [PubMed: 29109462]
45. Yamanaka M, Teranishi T, Kawagoe H, Nishizawa N. Optical coherence microscopy in 1700nm spectral band for high-resolution label-free deep-tissue imaging. Sci Rep 2016;6: 31715. [PubMed: 27546517]

46. Ishida S, Nishizawa N. Quantitative comparison of contrast and imaging depth of ultrahigh-resolution optical coherence tomography images in 800–1700nm wavelength region. Biomed Opt Express 2012;3(2):282–294. [PubMed: 22312581]

47. Kawagoe H, Ishida S, Aramaki M, et al. Development of a high powersupercontinuumsourceinthe1.7mmwavelengthregion for highly penetrative ultrahigh-resolution optical coherence tomography. Biomed Opt Express 2014;5(3):932–943. [PubMed: 24688825]

48. Srinivasan VJ. Optical coherence microscopy for deep tissue imaging of the cerebral cortex with intrinsic contrast. Opt Express 2012;20(3):2220–2239. [PubMed: 22330462]

49. Hoeling B, Fernandez A, Haskell R, et al. An optical coherence microscope for 3-dimensional imaging in developmental biology. Opt Express 2000;6(7):136–146. [PubMed: 19404345]

50. Hsiung P-L, Nambiar PR, Fujimoto JG. Effect of tissue preservation on imaging using ultrahigh resolution optical coherence tomography. J Biomed Opt 2005;10(6):64033.

51. Schmitt JM, Xiang SH, Yung KM. Differential absorption imaging with optical coherence tomography. J Opt Soc Am A 1998;15(9):2288–2296.

52. Kimura M, Tayama N, Chan RW. Geometrical deformation of vocal fold tissues induced by formalin fixation. Laryngoscope 2003;113(4):607–613. [PubMed: 12671415]

53. Stevens KA, Thomson SL, Jetté ME, Thibeault SL. Quantification of porcine vocal fold geometry. J Voice 2016;30: 416–426. [PubMed: 26292797]

54. Jiang JJ, Raviv JR, Hanson DG. Comparison of the phonation-related structures among pig, dog, white-tailed deer, and human larynges. Ann Otol Rhinol Laryngol 2001;110(12): 1120–1125. [PubMed: 11768701]

55. Wong BJ, Si MS, Cho C, Liaw LH, Neev J. XeCl laser surgery of the vocal cords: a histologic comparison with CO2 laser in a porcine model. Otolaryngol Head Neck Surg 1998;118(3 Pt 1): 371–375. [PubMed: 9527119]

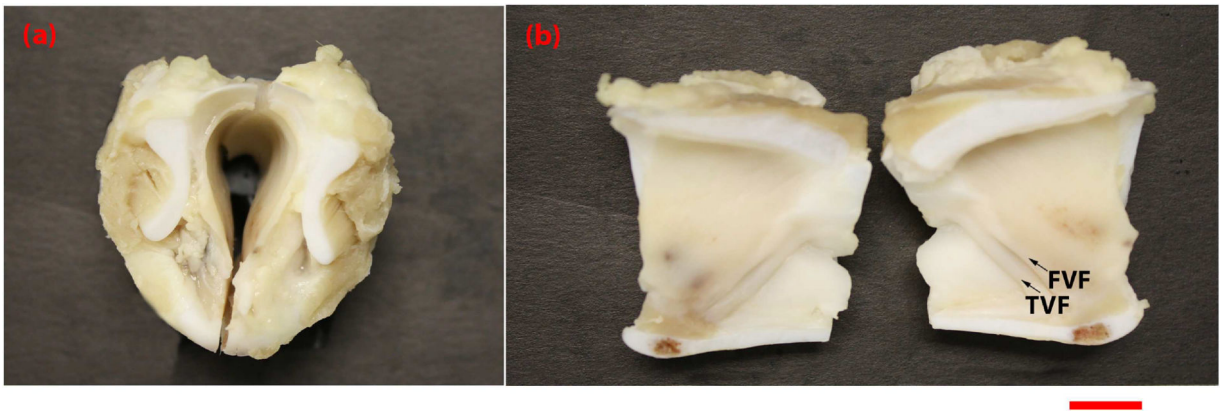

Fig. 1.

Photograph of formalin fixed porcine larynx imaged by OCT systems. This porcine larynx was freshly excised and fixed in formalin prior to imaging. (**a**) depicts the top down view of the bisected sample, (**b**) depicts the luminal surface of the larynx, with arrows indicating TVF=true vocal folds and FVF=false vocal folds. Scale bar indicates 1cm.

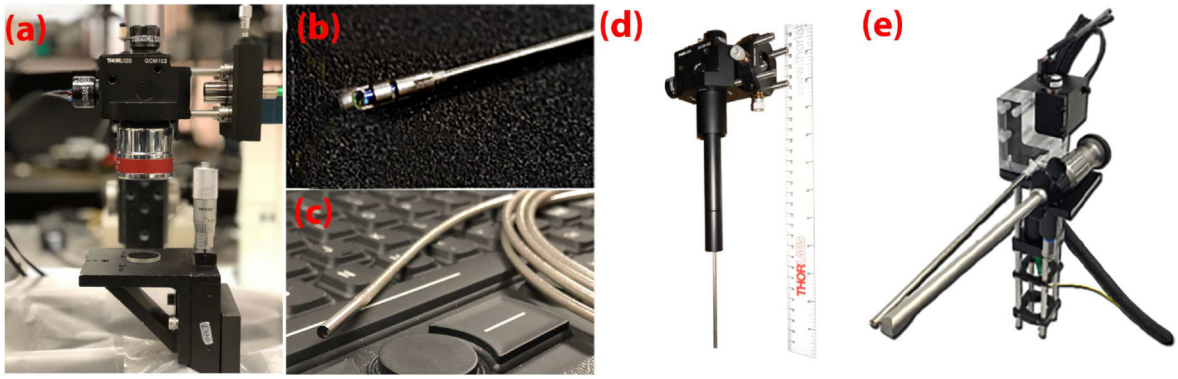

Fig. 2.

Photograph of probes from OCT systems. The various imaging probes utilized to image the vocal folds include the (**a**) SS-OCT 1310nm 200kHz VCSEL system and microscope, and SS-OCT 1700nm 90kHz system and microscope; (**b**) SS-OCT 1310nm 50kHz system and flexible side viewing endoscope; (**c**) TD-OCT 1310nm 254kHz and flexible forward viewing endoscope; (**d**) SS-OCT 1310nm 50kHz and rigid forward viewing endoscope; (**e**) SS-OCT 1310nm 200kHz and rigid forward viewing endoscope.

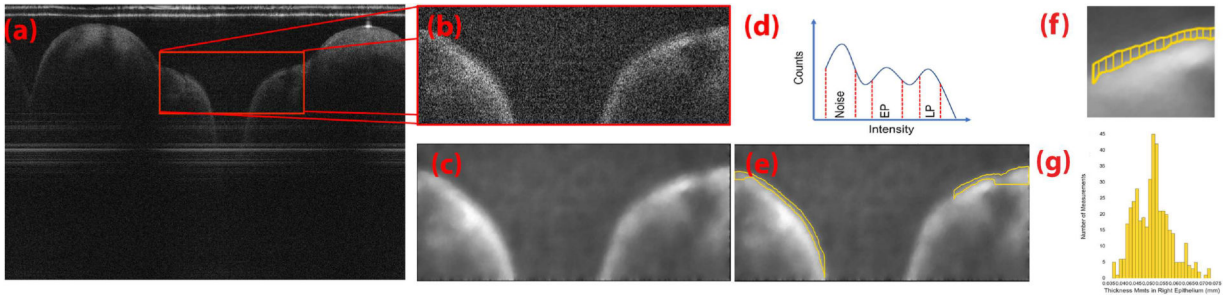

Fig. 3.

Processing algorithm for intensity thresholding segmentation and epithelium measurements. (**a**) A selection of an ROI was made on the original OCT image denoted by the red box.The (**b**) cropped ROI (**c**) is denoised and smoothed by total variation denoising with split-Bregman optimization. (**d**) Intensity histogram of the entire denoised image or B-scan was used to bin respectively for pixel intensities that belong to the image noise, epithelium and, lamina propria. (**e**) Pixel populations identified are then contoured using the marching squares algorithm. (**f**) Vertical distances between the top and bottom contour of the EP, shown in yellow. (**g**) Resulting histogram distribution of the measured EP thickness.

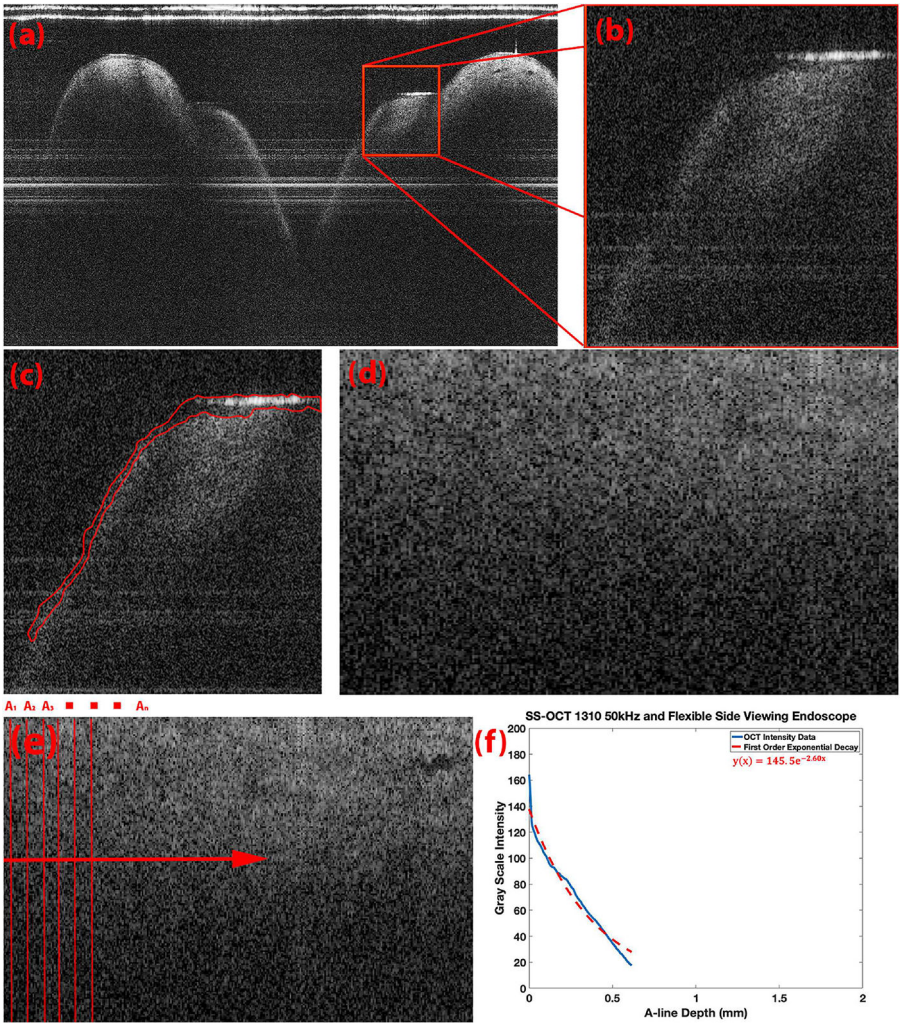

Fig. 4.

Processing algorithm for determination of alpha constants. (**a**) A representative OCTB-scan is cropped to a given ROI of the true vocal folds denoted by the red box (**b**) Resulting cropped OCT image containing the segment of interest (**c**) Epithelium is segmented and removed (**d**) Remaining lamina propria edge is then shifted to a horizontal line to simplify computation (**e**) All vertical A-lines in an image are averaged laterally (**f**) Blue: resulting laterally averaged OCT A-lines, Red: fitted first order exponential decay on the blue OCT depth resolved intensity.

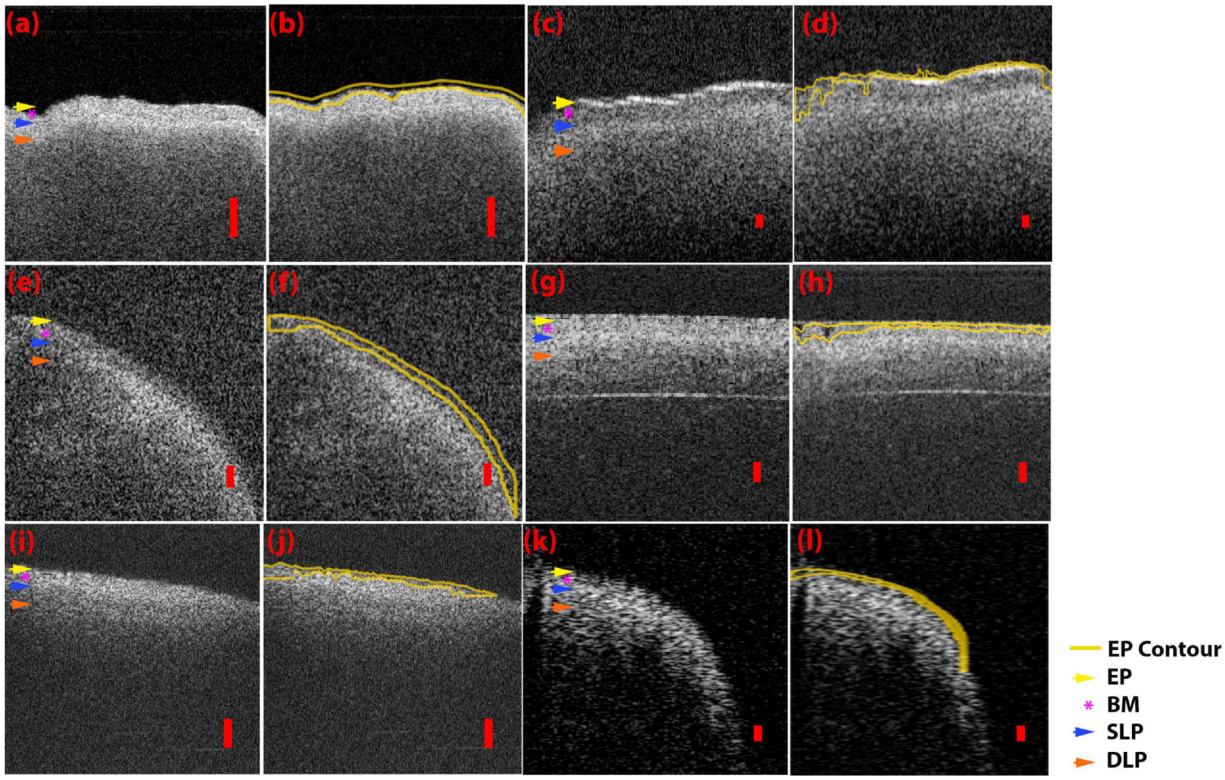

Fig. 5.

Intensity threshold contouring of the epithelium for each OCT system. Representative ROI and contoured ROI of (**a**,**b**) SS-OCT 1310nm 200kHz VCSEL system and microscope scanning probe, (**c**,**d**) SS-OCT 1700nm 90kHz system and microscope scanning probe, (**e**,**f**) SS-OCT 1310 50kHz system and flexible side viewing endoscope (**g**,**h**) TD-OCT 1310nm 254Hz system and flexible forward viewing endoscope (**I**,**j**) SS-OCT 1310nm 50kHz system and rigid forwarding viewing endoscope (**k**,**l**) SS-OCT 1310 nm 200 kHz VCSEL system and rigid side viewing endoscope. Yellow contour and yellow arrow denotes epithelium, purple asterisk denotes basement membrane, blue arrow denotes superficial lamina propria, and orange arrow denotes deep lamina propria. Red scale bars denote 200μm of axial distance.

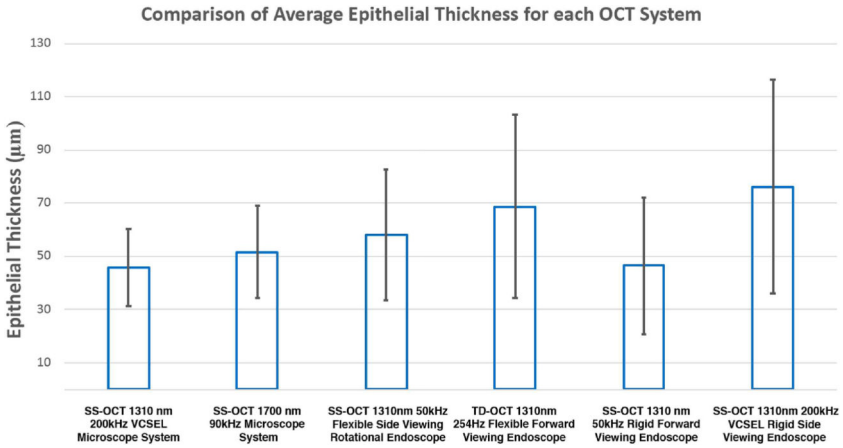

Fig. 6.

Comparison of average epithelial thickness for each OCT system. Bar graph of average epithelial thicknesses for each OCT system with corresponding standard error of the mean bars.

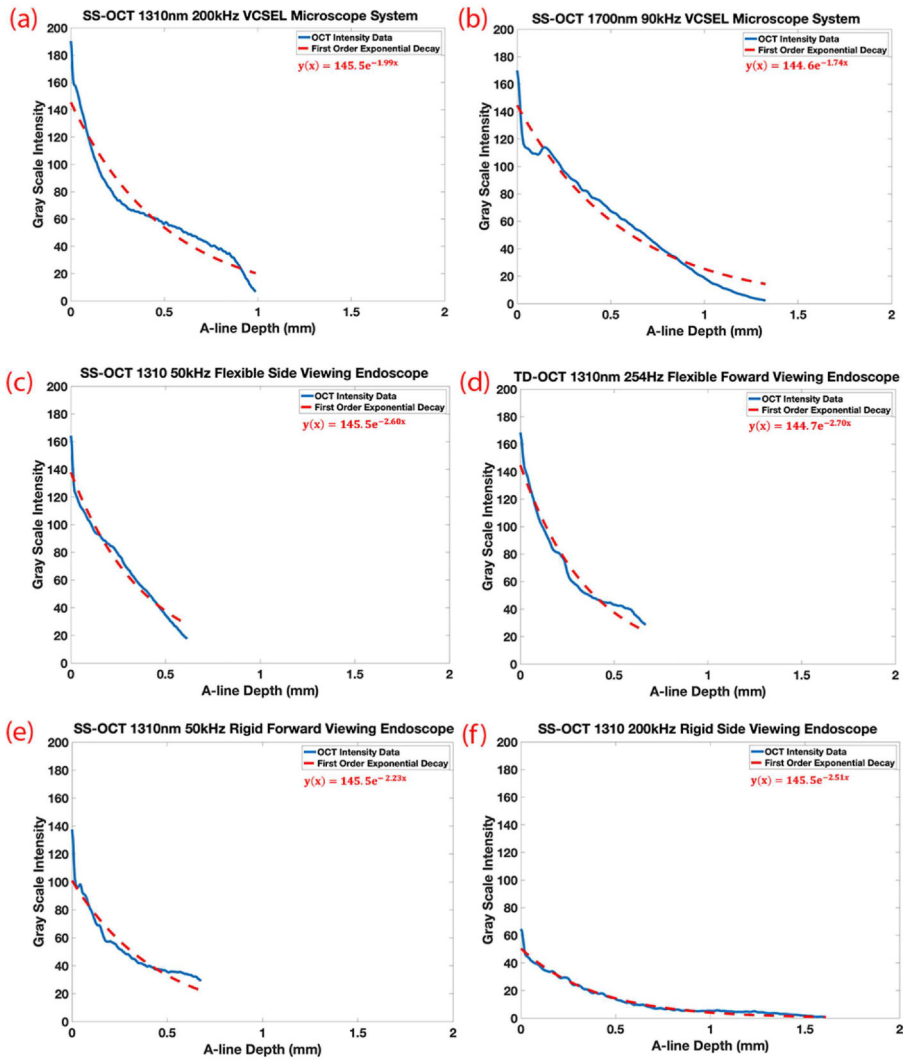

Fig. 7.

Average intensity based exponential decay curves and alpha constant of vocal folds imaged by each OCT system. Laterally averaged depth intensity and its exponential decay curves for the respective OCT systems and probes imaging the same fixed porcine larynx (**a**) SS-OCT 1310nm 200kHz VCSEL microscope system, (**b**) SS-OCT 1700nm 90kHz microscope system, (**c**) SS-OCT 1310nm 50kHz flexible side viewing endoscope, (**d**) TD-OCT 1310nm 254kHz flexible forward viewing endoscope, (**e**) SS-OCT 1310nm 50kHz rigid forward viewing endoscope, (**f**) SS-OCT 1310nm 200kHz rigid forward viewing endoscope. SS-OCT=swept-source OCT, VCSEL= vertical-cavity surface-emitting laser, TD-OCT=time-domain OCT.

Table 1.

Specifications of OCT Systems

OCT system type, center wavelength, A-line rate	Probe type	Working distance	Axial resolution	Lateral resolution	Pixel resolution	Imaging speed
SS-OCT, 1310nm, 200kHz VCSEL	Microscope scanner	35mm	5.8μm	22.5μm	3.8μm	200fps
SS-OCT, 1700nm, 90kHz	Microscope scanner	35mm	12μm	29.2μm	8.5μm	90fps
SS-OCT, 1310nm, 50kHz	Flexible side viewing rotational endoscope	7mm	10μm	102μm	4.8μm	50fps
TD-OCT, 1310nm, 254Hz	Flexible forward viewing endoscope	1.6mm	15μm	25μm	6.9μm	1fps
SS-OCT, 1310nm, 50kHz	Rigid forward viewing endoscope	8.5mm	9.8μm	5.4μm	4.8μm	50fps
SS-OCT, 1310nm, 200kHz VCSEL	Rigid side viewing endoscope	7–10cm	9.3μm	100μm	5.9μm	200fps

SS-OCT, swept-source OCT; VCSEL, vertical-cavity surface-emitting laser; fps, frames per second; TD-OCT, time-domain OCT.

Table 2.

Comparison of Images Obtained by OCT Systems

Imaging system	Probe type	Alpha (a) constants	EP/LP layer differentiation (visual assessment)	Visible basement membrane (visual assessment)
SS-OCT 1310nm 200kHz VCSEL	Microscope	−1.99	Not Visible	Visible
SS-OCT 1700nm 90kHz	Microscope	−1.74	Not Visible	Visible
SS-OCT 1310nm 50kHz	Flexible side viewing rotational endoscope	−2.60	Visible	Visible
TD-OCT 1310nm 254Hz	Flexible forward viewing endoscope	−2.70	Visible	Visible
SS-OCT 1310nm 50kHz	Rigid forward viewing endoscope	−2.23	Not Visible	Not Visible
SS-OCT 1310nm 200kHz VCSEL	Rigid side viewing endoscope	−2.51	Moderately Visible	Moderately Visible

SS-OCT, swept-source OCT; VCSEL, vertical-cavity surface-emitting laser; TD-OCT, time-domain OCT; EP, epithelium; LP, lamina propria.

Table 3.

Porcine Larynx Epithelium Measurements from Intensity Based Contouring

Imaging system	Probe type	Average epithelium thickness (μm)	Standard deviation (μm)
SS-OCT 1310nm 200kHz VCSEL	Microscope	45.73	14.34
SS-OCT 1700nm 90kHz	Microscope	51.58	17.30
SS-OCT 1310nm 50kHz	Flexible side viewing rotational endoscope	58.19	24.62
TD-OCT 1310nm 254Hz	Flexible forward viewing endoscope	68.76	34.45
SS-OCT 1310nm 50kHz	Rigid forward viewing endoscope	46.52	25.64
SS-OCT 1310nm 200kHz VCSEL	Rigid side viewing endoscope	76.27	40.02
Average epithelium thickness across six OCT systems		55.79	31.86